HHS Public Access

Author manuscript

Nat Med. Author manuscript; available in PMC 2019 April 23.

Published in final edited form as:

Nat Med. 2017 December ; 23(12): 1481–1487. doi:10.1038/nm.4428.

IRF3 and Type I Interferons Fuel a Fatal Response to Myocardial Infarction

Kevin R. King[1,2], **Aaron D. Aguirre**[2,3], **Yu-Xiang Ye**[2], **Yuan Sun**[2], **Jason D. Roh**[3], **Richard P. Ng Jr.**[2,4], **Rainer H. Kohler**[2], **Sean P. Arlauckas**[2], **Yoshiko Iwamoto**[2], **Andrej Savol**[5,6], **Ruslan I. Sadreyev**[5,7], **Mark Kelly**[8], **Timothy P. Fitzgibbons**[8], **Katherine A. Fitzgerald**[9], **Timothy Mitchison**[10], **Peter Libby**[11], **Matthias Nahrendorf**[2], and **Ralph Weissleder**[2,10]

[1]Department of Medicine/Cardiology and Bioengineering, University of California San Diego, La Jolla, CA, USA.

[2]Center for Systems Biology, Massachusetts General Hospital and Harvard Medical School, Simches Research Building, 185 Cambridge Street, Boston, MA, USA.

[3]Cardiology Division, Massachusetts General Hospital, Harvard Medical School, Boston, Massachusetts, USA.

[4]Harvard College, Cambridge, Massachusetts, USA.

[5]Department of Molecular Biology, Massachusetts General Hospital, Boston, Massachusetts, USA

[6]Department of Genetics, Harvard Medical School, Boston, Massachusetts, USA

[7]Department of Pathology, Massachusetts General Hospital and Harvard Medical School, Boston, Massachusetts, USA

[8]Department of Medicine, Cardiovascular Division, University of Massachusetts Medical School, Worcester, USA.

[9]Department of Immunology, University of Massachusetts Medical School, Worcester, MA, USA.

[10]Department of Systems Biology, Harvard Medical School, Boston, MA, USA.

[11]Cardiovascular Division, Department of Medicine, Brigham and Women's Hospital, Harvard Medical School, Boston, MA, USA.

Abstract

Corresponding author: Kevin R. King, MD, PhD, University of California San Diego, 9500 Gilman Dr. MC 0412, La Jolla, CA 92093, Tel: 617-869-9339, krking@ucsd.edu.

Author Contributions K.R.K. and A.D.A. designed and performed the experiments, analyzed the data, and wrote the manuscript; Y.-X.Y. designed and performed experiments, and analyzed data; M.K. performed myocardial infarction on WT, *IFNAR*$^{-/-}$, *and cGAS*$^{-/-}$ mice with T.P.F; Y.S. performed myocardial infarctions on WT and all other mouse strains; A.S. and R.I.S. performed bioinformatics analysis; Y.I. performed histologic analysis; R.P.N.Jr. performed biomolecular analysis; J.D.R. performed echocardiography and data analysis, R.H.K. performed confocal imaging, S.P.A. performed bone marrow derived macrophage experiments, T.M., K.A.F., and P.L. provided guidance on experimental design; and M.N. and R.W. designed experiments, analyzed data, and revised the manuscript. All authors reviewed results and commented on the manuscript.

The authors declare no competing financial interests.

Interferon regulatory factor 3 (IRF3) and type I interferons (IFNs) protect against infections[1] and cancer[2], but excessive IRF3 activation and type I IFN production cause auto-inflammatory conditions such as Aicardi Goutieres Syndrome[3,4] and STING-associated vasculopathy of infancy (SAVI)[3]. Myocardial infarction (MI) elicits inflammation[5], but the dominant molecular drivers of MI-associated inflammation remain unclear. Here, we show that ischemic cell death in the heart fuels a fatal response to myocardial infarction by activating IRF3 and type I IFN production. In mice, single cell RNA-Seq analysis of 4,215 leukocytes isolated from infarcted and non-infarcted hearts revealed that MI provokes activation of an IRF3-interferon axis in a distinct population of interferon inducible cells (IFNICs that were classified as cardiac macrophages). Mice genetically deficient in cGAS, its adaptor STING, IRF3, or the type I interferon receptor IFNAR exhibited impaired interferon stimulated gene (ISG) expression and, in the case of mice deficient in IRF3 or IFNAR, improved survival after MI as compared to controls. Interruption of IRF3-dependent signaling resulted in decreased cardiac expression of inflammatory cytokines and chemokines and decreased cardiac inflammatory cell infiltration, as well as in attenuated ventricular dilation and improved cardiac function. Similarly, treatment of mice with an IFNAR neutralizing antibody after MI ablated the IFN response and improved left ventricular dysfunction and survival. These results identify IRF3 and the type I interferon response as a potential therapeutic target for post-MI cardioprotection.

SUMMARY

The massive cell death that occurs during myocardial infarction releases self-DNA and triggers an interferon response in infiltrating leukocytes via a cGAS-STING-IRF3 pathway. In mice subjected to myocardial infarction, genetic disrupton of this pathway or antibody blockade of the type I interferon receptor improved heart function and survival.

Myocardial infarction (MI) causes massive synchronous cell death in the heart and catastrophically releases innate immune-stimulating damage associated molecular patterns (DAMPs). Although the molecular nature of the dominant MI-induced DAMPs remains undefined, these DAMPs are thought to be sensed by Toll like receptors (TLRs) of infiltrating cells and to fuel post-MI inflammation by activating the transcription factor NF-κB and expression of pro-inflammatory cytokines TNF-α, pro-IL1β, and IL6[6,7]. Unfortunately, despite the association between inflammation and poor clinical outcomes, efforts to limit post-MI- and heart failure-associated inflammation with steroidal or non-steroidal anti-inflammatory drugs that target NF-κB-dependent signaling have failed to show benefit[8]. Thus, an improved molecular understanding of MI danger signaling might enable more effective post-MI cardioprotection[8].

Cytosolic nucleic acid sensors initiate TLR-independent responses that protect against infection by invading pathogens[1,9]. For example, during viral or intracellular bacterial infection, the cytosolic DNA sensor cGAS detects pathogen DNA[10] and catalyzes the synthesis of the cyclic dinucleotide cGAMP[11], which signals via the adaptor STING[12], facilitates TBK1-dependent IRF3 activation[13], and orchestrates a gene expression program characterized by IFNβ production and the type I interferon response. Meanwhile, DNA abounds in every mammalian cell, but avoids spontaneous self-stimulation through nuclear and mitochondrial compartmentalization[14] and through enzymatic digestion by patrolling

endosomal and cytosolic DNases[15,16]. We hypothesized that the high levels of ischemic cell death during MI may disrupt DNA sequestration and liberate large quantities of self-DNA for cytosolic sensing, ultimately fueling a maladaptive IRF3-dependent innate immune response. To test this hypothesis, we studied IRF3 and the type I IFN response following permanent coronary ligation (MI) in mice.

Since IRF3 and type I IFNs lack established roles in ischemic heart disease, we first evaluated whether IRF3 is activated by MI in wild type (*WT*) mice. Despite the absence of infection in this setting, we detected increased levels of phosphorylated IRF3 (Fig. 1a, Supplementary Fig. 1a) and robust induction of prototypical IRF3-dependent cytokines (*Ifnb1*) and chemokines (*Cxcl10*) (Fig. 1b–c) on day 4 after MI; the increase in *Ifnb1* was detected as early as day 1 after MI (Supplementary Fig. 1b). In contrast to WT mice, IRF3 knockout mice ($Irf3^{-/-}$) showed a near complete abrogation of the MI-induced type I IFN response (Fig. 1b–c). Type I IFNs such as *Ifnb1* amplify immune responses by binding to cell-surface interferon alpha receptors (*Ifnar*), leading to induction of diverse effectors known as interferon stimulated genes (ISGs). Consistent with this concept, we detected marked increases in the levels of many ISGs in *WT* mice, but negligible induction in comparably treated $Irf3^{-/-}$ mice on day 4 after MI (Fig 1d). By comparison, Irf3 deficiency had a less severe effect on the mRNAs that encode prototypical NF-κB-dependent inflammatory cytokines such as *Tnf, Il1b*, and *Il6* (Supplementary Fig. 2). Genome-wide expression profiling of *WT* and $Irf3^{-/-}$ mice using RNA-seq confirmed these findings and showed that ISGs were among the most highly differentially expressed genes after MI ($P < 1\times10^{-12}$) (Fig. 1e, Supplementary Fig. 3).

To determine whether the interferon response is a specialized function of specific cells in the infarct, we performed single cell RNA-Seq profiling of 4,215 single cells using microfluidic inDrop barcoding (n=1858 and n=1654 CD45+ sorted infarct leukocytes from post-MI day 4 WT and $Irf3^{-/-}$ hearts, respectively, and n=703 unsorted cells from the ventricular apex of non-infarcted WT hearts). Unbiased clustering of the cells from post-MI WT hearts identified a unique population of interferon inducible cells (IFNICs) closely associated with mononuclear cell clusters (Fig. 1f). Based on analysis of marker gene expression as well as calculation of an IRF3 Score (*Ifit1, Ifit2, Ifit3*) defined as the summed expression of three genes previously identified direct IRF3-dependent genes, IFNICs were identified as specialized producers of ISGs and IRF3-dependent genes (Fig. 1g–h, Supplementary Tables 1–7)[17,18]. In contrast, we did not detect IFNICs by single cell analysis of post-MI day 4 $Irf3^{-/-}$ infarcts or of non-infarcted *WT* hearts (Supplementary Fig. 4).

Next, we explored which cell populations account for IRF3-dependent gene expression after MI using fluorescence activated cell sorting. Cells were sorted from the infarct region at day 4 based on cell surface CD45 and CD11b staining and were assessed for expression of IRF3-dependent genes. CD45+ and CD11b+ subpopulations, but not CD45- or CD11b- subpopulations, reliably expressed *Ifnb1* (Fig. 2a–b). Parabiosis experiments, in which $Irf3^{-/-}$ mice underwent coronary artery ligation after having been paired with either WT or $Irf3^{-/-}$ mice, revealed that, after MI, circulating cells enter the heart and significantly increase expression of IRF3-dependent genes (Fig. 2c). These data indicate that IFNICs are blood derived.

To study how IRF3-dependent responses are initiated after MI, we created a reporter mouse (Myh6Cre-mTmG) in which only cardiomyocytes express membrane EGFP (green), whereas all non-cardiomyocytes express membrane tdTomato (red)[19]. This approach enabled us to identify infiltrating cells with the greatest exposure to cardiomyocyte-derived DAMPs (red cells with green fluorescence above background). On day 4 after MI, we isolated $CD11b^+$ cells associated with cardiomyocyte debris by gating on red cells with GFP levels above a stringently defined background (Fig. 2d–h, Supplementary Fig. 5). This $CD11b^+GFP^+$ population consisted almost exclusively of $F4/80^{hi}Ly6C^{lo}$ cells (macrophages), which we termed post-phagocytotic macrophages (Fig. 2f). These $CD11b^+GFP^+$ cells expressed significantly more *Ifnb1* than did $CD11b^+GFP^-$ cells (Fig. 2g). In contrast, both $CD11b^+$ cell populations expressed similar amounts of ISGs (Fig. 2h). Together, these results indicate that DAMP sensing by infarct phagocytes leads to type I interferon production, which secondarily induces ISG expression in nearby cells, regardless of their direct association with the initiating cardiomyocyte DAMP. To visualize the spatial distribution of interferon-responsive cells, we created an interferon-inducible reporter mouse (*Mx1Cre mT/mG*) expressing membrane tdTomato (red) in all cells except those induced to express Cre recombinase by endogenous activation of the interferon-sensitive Mx1-promoter, which changes reporter expression to membrane EGFP (green)[4,19]. On day 4 after MI, reporter mice exhibited dense accumulation of green interferon-responsive cells throughout the infarct zone (Fig. 2i), but no green interferon-responsive cells were morphologically consistent with the large sarcomere-containing appearance of a typical cardiomyocyte, which suggests that non-myocytes are the interferon-responsive cell type.

We next investigated whether the interferon response impacted the extent and quality of immune cell infiltrate. Immunohistochemical staining and multi-photon autofluorescence microscopy showed reduced accumulation of leukocytes in the borderzone region in $Irf3^{-/-}$ compared to *WT* mice at day 4 after MI (Fig. 2j, Supplementary Fig. 6a–b). Using flow cytometry, we found that the decreased amount of infarct infiltrate in $Irf3^{-/-}$ compared to WT mice resulted from a decrease in the $F4/80^{low}Ly6C^{hi}$ pro-inflammatory monocyte population (Fig. 2k). By comparison, the size of the $F4/80^{hi}$ $Ly6C^{low}$ phagocytic macrophage population was only modestly affected. These observations are consistent with findings that, as compared to $Irf3^{-/-}$ mice, WT mice showed increased expression of cell surface leukocyte adhesion molecules and leukocyte recruitment chemokines, which facilitate leukocyte infarct infiltration (Supplementary Fig. 6c–d). Next, we examined expression in our single-cell RNA-Seq data of mononuclear cell surface markers recently linked to ontologic and phenotypic subsets of leukocytes. This analysis identified IFNICs as *Adgre1*+ (F4/80) *H2.Aa*+ (MHCII) *Ccr2*+ *Ly6c2*- (Ly6C) cells (Fig. 2l), classifying them as a monocyte-derived cardiac macrophage[20]. This cell population was not identifiable by analysis of the single-cell RNA-Seq data derived from leukocytes of $Irf3^{-/-}$ mice or of *WT* sham controls (Supplementary Fig. 4c–d). Taken together, these results suggest that interactions of infarct phagocytes with cardiomyocyte debris fuel IRF3-dependent leukocyte recruitment and amplify inflammation after MI.

We next sought to determine the dominant DAMP responsible for MI-induced IRF3 activation. Three adaptor proteins can activate IRF3[21]: TIR-domain-containing adapter inducing interferon beta (TRIF)[22], Mitochondrial antiviral-signaling protein (MAVS)[23], and

Stimulator of interferon genes (STING)[12,24] (Fig. 3a). By subjecting mice functionally deficient in each adaptor to MI, we found that *STING*$^{gt/gt}$ mice most closely replicate the *Irf3*$^{-/-}$ post-MI expression pattern: as compared to WT mice, *STING*$^{gt/gt}$ mice showed reduced *Ifnb1* expression and a near complete abrogation of *Cxcl10*, *Irf7*, and *Ifit1* expression despite no significant decreases in the expression of cytosolic DNA sensing molecules (Fig. 3b, Supplementary Fig. 2e–i).

Cytosolic double-stranded DNA (dsDNA) is the only endogenous DAMP known to activate IRF3 via the adaptor STING. It does so via the DNA sensor cyclic GMP-AMP synthase, cGAS (Fig. 3c). Indeed, *cGAS*$^{-/-}$ mice[10], like *Irf3*$^{-/-}$ and *STING*$^{gt/gt}$ mice, did not exhibit a significant induction of the type I interferon response after MI (Fig. 3d). Similarly, *Ifnar*$^{-/-}$ mice lacking the type I IFN receptor also showed no elevation in interferon stimulated gene expression after MI (Fig. 3d). Furthermore, we observed a substantial overlap between the genes most differentially expressed in *WT* as compared to *Irf3*$^{-/-}$ mice after MI and those previously found to be induced by mitochondrial DNA release[14], bacterial DNA secretion[25], or DNA accumulation due to absence of endogenous DNase activity[16,26] (Supplementary Fig. 3c–d). Together, these results identify the cytosolic DNA sensing pathway as being responsible for induction of an IRF3-dependent type I interferon response in the heart after MI.

To determine if ischemic injury disrupts intracellular compartmentalization and makes cardiomyocyte DNA available for sensing, we performed an ischemia-reperfusion procedure in which mice were subjected to 20 minutes of coronary ligation followed by reperfusion; the restoration of flow was used to allow delivery of DNA-binding-dependent fluorescent probes, PicoGreen or Sytox Orange. Using gated intravital microscopy in the beating heart, we found that the DNA probes localized exclusively to the nucleus of intact surviving cells, whereas they spread throughout the cytosol of injured cells (Fig. 3e–f, Supplementary Fig. 7).

Next, we devised an experiment to determine whether infiltrating cells access cardiomyocyte DNA in the infarct *in vivo*. Cardiomyocyte DNA was indelibly labeled in utero by injecting pregnant mice with the modified nucleotide EdU. When the offspring grew to adults, the location of the covalent DNA-bound EdU was visualized by bioorthogonal click chemistry. Cardiomyocytes, which proliferate rapidly in utero but minimally in adulthood, retain the label in adult mice, whereas highly proliferative hematopoietic-cells and their leukocyte progeny diluted the EdU to undetectable levels (Fig. 3g)[27]. When we challenged the labeled mice with MI, we found some EdU localized to the extranuclear space of infiltrating borderzone cells on day 4 after MI, but not to circulating cells of cytospun blood. For comparison, when we exposed bone marrow derived macrophages *in vitro* to EdU-labeled DNA extracted from the heart, we observed a similar distribution of EdU labeling of the macrophages, together with induction of type I interferon and ISG expression (Fig. 3h, Supplementary Fig. 8). Bone marrow derived macrophages from WT mice strongly express type I interferons in response to DNA. Macrophages from cGAS, STING or IRF3 deficient mice were unable to mount a similar response (Supplementary Fig. 9). Together this indicates macrophages can access extracellular DNA and produce type I interferons in a cGAS-, STING-, and IRF3-dependent fashion. Together, these findings suggest that

ischemic cells in the heart release DNA that provokes infarct phagocytes to induce a cGAS- and IRF3-dependent type I interferon response.

To determine the functional significance of MI-induced IRF3-activation, we compared survival, ventricular remodeling, and contractile function after MI between WT mice and mice with impaired interferon signaling. Despite closely matched baseline echocardiographic parameters and MRI-assessed infarct size (Supplementary Fig. 10a–d), we observed substantial differences in ventricular remodeling and survival between WT mice and *Irf3*$^{-/-}$, *Ifnar*$^{-/-}$ or *cGAS*$^{-/-}$ mice (Fig. 4a–l) Consistent with prior reports[28], 61% (35/57) of *WT* male mice survived after MI; these mice showed ventricular rupture between days 4–6 (Fig 4a). In contrast, *Irf3*$^{-/-}$ and *Ifnar*$^{-/-}$ mice showed virtually completely protection from death with 98% survival (44/45) and 100% (31/31) respectively over the 2 weeks of observation following coronary artery occlusion. *cGAS*$^{-/-}$ mice also showed a significant, although less striking, protection (39/47). In contrast, Sting$^{gt/gt}$ mice showed a nonsignificant decrease in mortality (Supplementary Fig. 11), suggesting that other innate immune sensors might also participate in IRF3 activation after MI. We also evaluated the effects of interferon signaling on ventricular dilation and contractile function, parameters that in humans predict symptoms and outcomes in heart failure. Longitudinal assessment of ventricular size at days 4, 7, and 21 revealed less dilation of *Irf3*$^{-/-}$ mice compared to *WT* mice (Supplementary Fig. 12). Echocardiographic and cardiac MRI evaluation on days 4 and 21 after MI revealed significantly less chamber dilation and greater preservation of contractile function in *cGAS*$^{-/-}$, *Irf3*$^{-/-}$, and *IFNAR*$^{-/-}$ mice as compared to WT mice (4b-l). No substantial differences in coronary vascular anatomy, spontaneous reperfusion, or recruitment of collateral vessels could be identified between *WT* and *Irf3*$^{-/-}$ mice to explain the differences in ventricular dilation, contractile function, and survival (Supplementary Fig. 10e–f).

To test the translational potential of these findings, we treated *WT* mice with an IFNAR neutralizing antibody at 12 and 48 h after MI. Antibody treatment abrogated ISG expression and improved ventricular size, contractile function, and survival (Fig. 4m–p). This demonstrates that transient inhibition with anti-interferon therapy initiated after coronary occlusion protect the recently infarcted ventricle.

In summary, our findings highlight overlap between the protective host response to pathogens and its deleterious consequences when activated in the context of sterile ischemic injury. We show that MI, which causes ischemic cell death in the heart, activates IRF3 and the type I IFN response in a new subpopulation of cardiac macrophages we call IFNICs. Pathway activation depends on cytosolic DNA sensing and disruption of the pathway, genetically or pharmacologically, reduces inflammation and injury while improving ventricular function and survival. (Fig. 5q).

Therapeutically, cancer immunotherapy and vaccine adjuvants aim to boost innate immunity[29–31]. Here, we suggest that transient inhibition of the interferon-dependent innate immune response to ischemic cell death could reduce inflammation and limit the adverse ventricular remodeling that leads to clinical heart failure. Humans tolerate anti-interferon biologics that are in clinical development for rheumatologic indications[32–34], suggesting the

feasibility of targeting the interferon response in MI. The profound effects of IRF3 and the type I interferon response on inflammation and ventricular remodeling after myocardial infarction expand the role of this response beyond host defense and autoimmunity and support its exploration as a new target for post-MI cardioprotection.

Materials and Methods

Animals

Adult C57BL/6J (*WT*, stock 000664), type I interferon-inducible Cre expressing B6.Cg-Tg(Mx1-cre)1Cgn/J (*Mx1-Cre*, stock 003556)[19], cardiomyocyte-specific Cre expressing B6.FVB-Tg(Myh6-cre)2182Mds/J (*Myh6-Cre*, stock 011038), Gt(ROSA)26Sor$^{tm4(ACTB-tdTomato,-EGFP)Luo}$/J (*mTmG*, stock 007576)[35], MAVS deficient B6;129-Mavs,tm1Zjc>/J (*MAVS*$^{-/-}$, stock 008634)[36], TRIF functionally deficient C57BL/6J-*Ticam1*^{Lps2}/J (*TRIF*$^{Lps2/Lps2}$, stock 005037)[37], STING functionally deficient C57Bl/6J-Tmem173<gt>/J (*STING*$^{gt/gt}$, stock 017537)[24], and cGAS deficient B6(C)-Mb21d1,tm1d(EUCOMM)Hmgu>/J (*cGAS*$^{-/-}$ mice were purchased from the Jackson Laboratory (stock 026554) or obtained from Fitzgerald lab after derivation from cryopreserved embryos obtained from the European Conditional Mouse Mutagenesis Program (EUCOMM)). IRF3$^{-/-}$ mice[38] were a generous gift from Tadatsugu Taniguchi and provided by Michael Diamond. IFNAR knockout mice (*IFNAR*$^{-/-}$) were originally from J. Sprent and were backcrossed for 12 generations at the University of Massachusetts Medical School and provided by Kate Fitzgerald. Genotyping was performed in-house using methods recommended by Jackson Laboratory, or by Transnetyx. All experiments were performed with 10 to 25-week-old animals and were carried out using age and gender matched groups without randomization. All mice were maintained in a pathogen-free environment of the Massachusetts General Hospital of University of Massachusetts animal facilities, and all animal experiments were approved by the Subcommittee on Animal Research Care at Massachusetts General Hospital or University of Massachusetts.

Myocardial Infarction and Cardioprotective Therapy

Mice were intubated and ventilated with 2% isoflurane. After exposing the heart via thoracotomy at the fourth left intercostal space, the left coronary artery was permanently ligated with an 8–0 nylon monofilament suture. The thorax was closed with a 5–0 suture. Mice were treated with buprenorphine for analgesia on the day of surgery and twice daily thereafter for 72 hours. For cardioprotection experiments, mice were treated with two intraperitoneal doses of 500 μg of MAR1–5A3 IFNAR neutralizing antibody (BioXCell) at 8–12 hours and at 48 hours after permanent coronary ligation. Surgeries were performed in a blinded fashion unless genotype was obviated by unavoidable ascertainment of features such as coat color.

Parabiosis

Mice were joined in parabiosis as previously described.[39] Mice were anesthetized with 2% isofluorane (2L/min O2). Briefly, after shaving the corresponding lateral aspects of each mouse, matching skin incisions were made from behind the ear to the tail of each mouse, and the subcutaneous fascia was bluntly dissected to create ~0.5 cm of free skin. The

scapulas were sutured using mono-nylon 5.0 (Ethicon, Albuquerque, NM), and the dorsal and ventral skins were approximated by continuous suture. All mice undergoing parabiosis surgeries were injected twice daily with buprenorphine (0.1mg/kg i.p.) for three days beginning on the day of surgery. Mice were joined for intervals of 2 weeks before proceeding with coronary ligation.

Blood and Heart Tissue Processing

Blood was collected by cardiac puncture. The cellular fraction was collected into EDTA-containing tubes (Sigma) and erythrocytes were eliminated using red blood cell lysis buffer (BioLegend). Heart tissue was collected by incising the right atrium and perfusing 10 mL of ice-cold saline into the left ventricular apex. Heart tissue was then removed and used for one of several assays detailed below. It was either imaged grossly, embedded in OCT (Sakura, Finetek) for frozen sectioning and immunohistochemical staining, placed in RNA Later (Qiagen) for RNA extraction and gene expression analysis, snap frozen in liquid nitrogen for protein analysis, fixed for 2 hours in 4% paraformaldyhyde for whole mount immunofluorescence staining, or freshly cut into short axis sections using a commercial heart slicer (Zivic Instruments) and placed between glass coverslips for immediate *ex vivo* imaging of genetically encoded fluorescence or endogenous autofluorescence. To obtain single cell suspensions for surface immunostaining, flow cytometric analysis, and FACS sorting, hearts were enzymatically digested for 1 hour under continuous agitation in 450 U/ml collagenase I, 125 U/ml collagenase XI, 60 U/ml DNase I, and 60 U/ml hyaluronidase (Sigma) for 1 hour at 37°C, and filtered through a 40 μm nylon mesh in FACS buffer (DPBS with 2.5% bovine serum albumin) for enumeration by flow cytometry. For single cell RNA-Seq, the enzymatic digestion was limited to 45 minutes.

Flow cytometry and Cell sorting

Isolated cells from enzymatically digested hearts were stained at 4°C in FACS buffer with mouse hematopoietic lineage markers including phycoerythrin (PE) or avidin-conjugated anti-mouse antibodies directed against B220 (BioLegend, clone RA3–6B2), CD49b (BioLegend, clone DX5), CD90.2 (BioLegend, clone 53–2.1), Ly6G (BioLegend, clone 1A8), NK1.1 (BioLegend, clone PK136) and Ter119 (BioLegend, clone TER-119). Secondary staining of leukocyte subsets was performed using CD11b (BioLegend, clone M1/70), CD11c (BioLegend, clone N418), CD45.2 (BioLegend, clone 104), F4/80 (Biolegend, clone BM8) and/or Ly6C (BioLegend, clone HK1.4 or BD Bioscience, clone AL-21). Neutrophils were identified as $(B220/CD49b/CD90.2/Ly6G/NK1.1/Ter119)^{high}$ $(CD45.2/CD11b)^{high}$. Monocytes were identified as $(B220/CD49b/CD90.2/Ly6G/NK1.1/Ter119)^{low}$ $(CD45.2/CD11b)^{high}$ and sub-classified as pro-inflammatory monocytes $F4/80^{low}Ly6C^{high}$ or macrophages $F4/80^{high}Ly6C^{low/int}$. Flow cytometry was performed on an LSRII (BD Biosciences) and analyzed with FlowJo software (Tree Star). Single cells from specific populations were collected for subsequent bimolecular analysis by FACS-sorting using a FACSAria II cell sorter (BD Biosystems). Single cell RNA-Seq samples were stained with Hoechst to exclude dead cells. Noninfarcted samples were unsorted. Infarcted samples were sorted for CD45+ cells only.

Quantitative real-time PCR (qPCR)

Total RNA was extracted from whole infarct tissue or FACS sorted cells using the RNeasy Mini or Micro kit (Qiagen) respectively according to the manufacturer's protocol. First-strand cDNA was synthesized using the High-Capacity RNA-to-cDNA kit (Applied Biosystems) according to the manufacturer's instructions. TaqMan gene expression assays (Applied Biosystems) were used to quantify target genes (*Ifnb1*, Mm00439546_s1; *Cxcl10*, Mm00445235; *Irf7*, Mm00516793_g1; *Ifit1*, Mm00515153_m1; *Ifit2*, Mm00492606_m1; *Ifit3*, Mm01704846_s1; *Oasl2*, Mm01201449_m1; *Rsad2*, Mm00491265_m1; *Tnf*, Mm00443258_m1; *Il1b*, Mm00434228_m1 *Il6*, Mm00446190_m1; *Mb21d1*, Mm01147496_m1; *Tmem173*, Mm01158117_m1; *Irf3*, Mm00516784_m1; *Ifnar2*, Mm00494916_m1). Relative changes were normalized to *Gapdh* mRNA using the $2^{-\Delta\Delta CT}$ method.

Genome-wide RNA Sequencing and Analysis

Total RNA from infarct tissue was isolated from *WT* and *Irf3*$^{-/-}$ mice on day 4 after MI. RNA-Seq libraries were constructed from polyA-selected RNA using the NEBNext Ultra Directional RNA library prep kit (Illumina, New England Biolabs) and sequenced on an Illumina HiSeq2500 instrument, resulting in approximately 41 million reads per sample on average. Transcriptome mapping was performed with STAR version 2.3.0[40] using the Ensembl 67 release exon/splice-junction annotations. Approximately 70–80% of reads mapped uniquely. Read counts for individual genes were produced using the unstranded count feature in HTSeq v.0.6.0[41]. Differential expression analysis was performed using the exactTest routine of the edgeR package[42] after normalizing read counts and excluding genes with low counts (cpm < 1 for 3 or more samples)[43]. Differentially expressed genes were defined based on the criteria of >2-fold change in expression value and false discovery rates (FDR) < 0.05. Functional annotation was performed using QIAGEN's Ingenuity Pathway Analysis (Supplementary Fig. 2a) (IPA, QIAGEN Redwood City, www.giagen.com/ingenuity) and the DAVID tool (Supplementary Fig. 2b)[44,45]. Published studies implicating cytosolic DNA sensing as the primary immune stimulus[14,16,25,26,46,47] were compared to the differentially expressed gene list determined by RNA-seq analysis of WT and IRF3$^{-/-}$ mice collected on day 4 after MI.

Microfluidic inDrop Single Cell RNA-Seq

Single cell RNA-Seq was performed by microfluidic inDrop encapsulation, barcoding, and library preparation, as previously described[48,49]. Paired end sequencing was performed on an Illumina Hiseq 2500 instrument. Low level analysis, including demultiplexing, mapping to a reference transcriptome (Ensembl Release 85 - GRCm38.p5), and eliminating redundant UMIs, was performed according to custom inDrops software (URL: https://github.com/indrops/indrops) [accessed April, 2017]. Mitochondrial, ribosomal, and hemoglobin genes were depleted bioinformatically, and clustering, dimensional reduction, and visualization was performed using the Seurat v1.4 software package in R with the following customization[50]. We considered cells expressing at least 200 genes, scaled to a total of 1×10^4 total molecules per cell, and log normalized the data. The gene space was limited to over-dispersed high variability genes. Linear dimensional reduction was performed with

principal component analysis. Unsupervised clustering was performed according to the default Seurat implementation of a community detection approach. Marker gene sets and associated p values were determined by differential expression using the Seurat implementation of the LRT test based on zero-inflated data. Cell and cluster proximity were visualized by projecting onto a 2D space using tSNE. Clusters were visualized using heatmaps of genes x clustered single cells and violin plots depicting expression probability densities for each cluster. To determine single cell IRF3 scores, we summed the counts for the directly IRF3-dependent genes, *Ifit1*, *Ifit2*, and *Ifit3*.

Histology and Immunohistochemistry

After removing contaminating blood by retrograde perfusion of the hearts from the ventricular apex with 10 ml of ice-cold PBS, hearts were embedded in OCT (Sakura Finetek) and flash-frozen in a 2-methylbutane bath on dry ice. OCT-embedded hearts were cut into serial 6 μm thick short axis sections and stained with hematoxylin and eosin or Masson's Trichrome (Sigma-Aldrich) according to the manufacturer's instructions. Sections were stained using the following primary antibodies to identify cell and biochemical features: neutrophils, monocytes, and macrophages (CD11b, M1/70, BD Biosciences); monocytes and macrophages (MOMA-2, MCA519G, AbD Serotec); and collagen deposition (Collagen I, ab32386, Abcam). Biotinylated anti-rat IgG (for MOMA-2) and anti-rabbit IgG (for Collagen I) were used for as a secondary antibody for immunohistochemical staining. Slides were scanned by a digital slide scanner, NanoZoomer 2.0-RS in 40x high resolution mode (Hamamatsu, Japan) or imaged on an Olympus FV1000 or a Nikon 80i fluorescence microscope and processed with ImageJ software using the Fiji package. The area of positive staining was quantified using custom semi-automated image analysis routines and at least five high power fields were analyzed per section and per animal.

Cardiomyocyte DNA Labeling and Detection

Pregnant mice were injected with 50 μL of 10 mM EdU (Thremofisher) on days 12, 16, and 20 post-conception. Hearts were perfused, sectioned, and fluorescently labeled for visualization with Alexa Fluor 647 azide using commercial copper-catalyzed covalent azide-alkyne click chemistry according to the manufacturer's protocol Sections were counterstained with Hoechst nuclear stain. Cardiomyocyte nuclei were confirmed to be EdU positive immediately after birth and at 10 weeks prior to MI. EdU-negativity of leukocytes from RBC lysed blood that was cytospin-deposited on a slide was confirmed in 10 week old adult mice.

Bone Marrow Derived Macrophage Stimulation with DNA

For *in vitro* stimulation with heart-derived EdU-labeled DNA, the above in utero EdU loading method was used to pre-label mouse heart DNA. Adult mouse hearts were harvested and perfused with cold PBS as above. DNA was extracted using a DNeasy kits (Qiagen) according to the manufacturer's recommendations. Isolated double stranded DNA was complexed with Lipofectamine LTX (ThermoFisher) at a 3:2 ratio of LTX (μL) to DNA (μg) for stimulation. Bone marrow derived macrophages (BMDM) were isolated from femurs of wild type mice and were allowed to differentiate in DMEM supplemented with 10% fetal bovine serum supplemented with 10 ng/mL M-CSF (Peprotech) for 1 week. The resulting

cells were stimulated with LTX alone (control) or LTX and DNA. After 24 hours, BMDM were lysed and RNA extracted into RLT buffer (Qiagen). RNA was isolated and quantitative RT-PCR performed as detailed above. In other experiments, BMDMs from cGAS$^{-/-}$, STING$^{gt/gt}$, and IRF3$^{-/-}$ mice were stimulated with medium alone, 2'3'cGAMP (10 μg/ml) (InvivoGen), Poly(I:C) (500 ng/mL) (InvivoGen), or 5 μg of herring testis DNA (Sigma) with LTX in 2 mL per well of a 6 well plate. RNA was extracted and quantified by qPCR as above.

Protein Analysis Western Blot and ELISA

Heart tissue protein was extracted in RIPA lysis buffer (Pierce) supplemented with protease/phosphatase inhibitor cocktail (Cell Signaling). Total protein concentration was quantified using BCA assay (Pierce). Lysates were denatured and subjected to gel electrophoresis using NuPAGE Novex Gel system (Life Technologies) and blotted on nitrocellulose membrane using iBlot Gel Transfer system (Life Technologies) according to the manufacturer's instructions. Blotting was performed with rabbit anti-mouse total IRF3 (Cell Signaling, #4302, Clone D83B9, used at 1:1000 dilution) and Phospho-IRF3 (Ser396) (Cell Signaling, #4947, Clone 4D4G, used at 1:1000 dilution). Loading control was blotted with goat anti-mouse GAPDH antibody (R&D Systems, P04406, used at 1:1000 dilution). Blots were visualized by labeling with HRP-coupled anti-rabbit and anti-goat secondary antibodies (Pierce, used at 1:5000) and incubating with chemiluminescent substrate (Pierce) administered. Gels were developed on a Kodak automated developer and quantified using densitometry with ImageJ. Quantification of CXCL10 protein was performed using an ELISA kit (R&D Systems, MCX100) according to manufacturer recommendations.

Coronary Perfusion Analysis

To visualize the coronary anatomy, high molecular weight >10kDa FITC dextran (Sigma) was injected into the tail vein and the anterior wall of the left ventricular was visualized on an OV110 (Olympus) microscope through a widely separated median sternotomy. To assess reperfusion after coronary ligation, 10 μm diameter fluorescent microspheres (Life Technologies, FluoSpheres, F8831) were injected into the left ventricular apex immediately after coronary ligation to delineate the initial territory deprived of blood flow. At the time of harvest, fluorescent microspheres of a second non-spectrally overlapping wavelengths (488nm and 647nm) were injected into the left ventricular apex and 1 mm thick short axis sections of the heart were made using a heart slicer (Zivic). Heart sections were then imaged on an Olympus FV1000 laser scanning confocal microscopy. Territory containing only the second and not the first microspheres was interpreted as reperfused territory and was reported as the fraction of total infarct.

Ex Vivo and Intravital Microscopy

After mouse intubation and ventilation with 2% isoflurane, the beating heart was exposed by median sternotomy and the heart was stabilized using a 3D printed tissue imaging stabilizer and prospective cardiac gating routine[51,52]. DAPI and the double-stranded DNA-specific (dsDNA) fluorescent probes Quant-iT PicoGreen (Thermofisher) or SYTOX Orange Nucleic Acid Stain (Thermofisher) were prepared in PBS and administered topically or by intravenous tail vein injection to identify dsDNA in the myocardium after ischemic injury.

PicoGreen was applied topically at 1:100 dilution in PBS to the infarcted area 20 minutes after permanent left coronary ligation. Sytox Orange was administered by intravenous injection after ischemia/reperfusion injury; the left coronary artery was ligated for 20 min and the ligation was then released. Sytox Orange was prepared at 1:50 dilution (2 μL stock in 100 μL PBS), injected immediately after reperfusion, and fluorescent probe uptake was imaged over time using two-photon microscopy. Fluorescence was quantified along line scans manually drawn orthogonal to the long axis of each myocyte at the level of the nucleus. *Ex vivo* imaging was performed by flushing the heart as detailed above, creating short axis cuts using a commercial heart slicer (Zivic). Imaging was performed using an Olympus FV1000MPE multi photon microscope with 750 nm excitation and two channel detection.

Echocardiography

Transthoracic echocardiography was performed on awake echo-probe conditioned mice before MI and on days 4 and 21 after MI in un-anesthetized mice using a Vivid E90 system (GE Healthcare) equipped with an L8–18i-D linear array transducer (15 MHz frequency). Parasternal short- and long-axis images were acquired at a depth of 10 mm using both M-mode and 2D-mode imaging at 250 and 605 frames per second, respectively. Image analysis was performed off-line using EchoPAC PC software (GE Healthcare, version 113). End-diastolic and end-systolic left ventricular internal diameters (LVIDd and LVIDs, respectively) were measured at the maximal and minimal diameters acquired from the parasternal short-axis images at a level selected for visualization of the papillary muscle. Fractional shortening (FS) was determined by calculating the change in left ventricular internal dimensions between end-diastole and end-systole normalized to end-diastolic dimension (LVIDd-LVIDs)/LVIDd.

Cardiac Magnetic Resonance Imaging (MRI)

Cardiac MRI was performed on days 1, and 21 after coronary ligation. Cine images of the left ventricular short axis were obtained using a 7 Tesla horizontal bore Pharmascan (Bruker) and a custom-built mouse cardiac coil in birdcage design (Rapid Biomedical). Acquisition was ECG triggered and respiratory gated using a fast low angle shot sequence. The echo time was 2.7ms, and the flip angle was 30 degrees (60 degrees for delayed enhancement imaging after intravenous injection of Gd-DTPA for measurement of infarct size). Images were analyzed using Segment software (http://segment/heiberg.se). Infarct size was determined by summing the % myocardial mass enhanced by gadolinium on serial short axis sections quantified at end-diastole. Ejection fraction was determined by calculating the change in ventricular volume between end-diastole and end-systole normalized to end-diastolic volume.

Statistics

Statistical analysis was performed using GraphPad Prism software. All data are represented as mean values +/− standard error of mean unless indicated otherwise. A statistical method was not used to predetermine sample size. For two-group comparisons, a 2-tailed Student's *t*-test was applied if the D'Agostino-Pearson normality test was not rejected at 0.05 significance; otherwise, a 2-tailed Mann-Whitney *U* test for nonparametric data was used.

All analysis except sorted cells were unpaired. For sorted cell samples, paired analysis was used to compare subpopulations from each mouse. For survival studies, mice dying within 24 hours of LAD ligation surgery (<10% in all genotypes studied) were pre-specified as purely technical failures and excluded from subsequent analysis per protocol. Statistical significance of Kaplan-Meier survival curves were assessed with a Mantel-Cox test. *P* values are indicated by *P* values less than 0.05 were considered significant and are indicated by asterisks as follows: *p<0.05, **p<0.01, ***p<0.001, ****p<0.0001.

Supplementary Material

Refer to Web version on PubMed Central for supplementary material.

Acknowledgements

We thank T. Taniguchi and M. Diamond for their gift of the IRF3$^{-/-}$ mice; P. Dutta, H. Sager, M. Hulsman, G. Courties, R. Giedt, and K. Yang for helpful discussions and technical assistance, B. Tricot for technical assistance with cardiac MRI as part of the Molecular Imaging Program core; the HSCI flow cytometry core, the MGH next generation sequencing core, the National Mouse Metabolic Phenotyping Center at UMass funded by an NIH 2U2C-DK093000, and the Single Cell Core at Harvard Medical School. The work was funded by NIH-NHLBI T32HL007604, HMS LaDue Fellowship, AHA17IRG33410543(K.R.K), and NIH-NHLBI K99HL129168 and R00HL129168 (K.R.K.); AHA14FTF20380185 (A.D.A.); AHA16FTF29630016 and Yeatts Fund for Innovative Research (J.D.R.); AHA16POST27030088, Deutsche Herzstiftung S/05/12 (Y.-X.Y.); R01HL117829 (M.N.); 5R01HL122208 (R.W.).

References

1. Goubau D, Deddouche S & Reis e Sousa C Cytosolic sensing of viruses. Immunity 38, 855–869 (2013). [PubMed: 23706667]
2. Woo SR et al. STING-dependent cytosolic DNA sensing mediates innate immune recognition of immunogenic tumors. Immunity 41, 830–842 (2014). [PubMed: 25517615]
3. Liu Y et al. Activated STING in a vascular and pulmonary syndrome. N Engl J Med 371, 507–518 (2014). [PubMed: 25029335]
4. Gall A et al. Autoimmunity initiates in nonhematopoietic cells and progresses via lymphocytes in an interferon-dependent autoimmune disease. Immunity 36, 120–131 (2012). [PubMed: 22284419]
5. Swirski FK & Nahrendorf M Leukocyte behavior in atherosclerosis, myocardial infarction, and heart failure. Science 339, 161–166 (2013). [PubMed: 23307733]
6. Frangogiannis NG The inflammatory response in myocardial injury, repair, and remodelling. Nat Rev Cardiol 11, 255–265 (2014). [PubMed: 24663091]
7. Mann DL Innate immunity and the failing heart: the cytokine hypothesis revisited. Circ Res 116, 1254–1268 (2015). [PubMed: 25814686]
8. Heusch G Cardioprotection: chances and challenges of its translation to the clinic. Lancet 381, 166–175 (2013). [PubMed: 23095318]
9. Cai X, Chiu YH & Chen ZJ The cGAS-cGAMP-STING pathway of cytosolic DNA sensing and signaling. Mol Cell 54, 289–296 (2014). [PubMed: 24766893]
10. Sun L, Wu J, Du F, Chen X & Chen ZJ Cyclic GMP-AMP synthase is a cytosolic DNA sensor that activates the type I interferon pathway. Science 339, 786–791 (2013). [PubMed: 23258413]
11. Wu J et al. Cyclic GMP-AMP is an endogenous second messenger in innate immune signaling by cytosolic DNA. Science 339, 826–830 (2013). [PubMed: 23258412]
12. Ishikawa H, Ma Z & Barber GN STING regulates intracellular DNA-mediated, type I interferon-dependent innate immunity. Nature 461, 788–792 (2009). [PubMed: 19776740]
13. Fitzgerald KA et al. IKKepsilon and TBK1 are essential components of the IRF3 signaling pathway. Nat Immunol 4, 491–496 (2003). [PubMed: 12692549]

14. West AP et al. Mitochondrial DNA stress primes the antiviral innate immune response. Nature 520, 553–557 (2015). [PubMed: 25642965]
15. Gao D et al. Activation of cyclic GMP-AMP synthase by self-DNA causes autoimmune diseases. Proc Natl Acad Sci U S A 112, E5699–705 (2015). [PubMed: 26371324]
16. Yoshida H, Okabe Y, Kawane K, Fukuyama H & Nagata S Lethal anemia caused by interferon-beta produced in mouse embryos carrying undigested DNA. Nat Immunol 6, 49–56 (2005). [PubMed: 15568025]
17. Andersen J, VanScoy S, Cheng TF, Gomez D & Reich NC IRF-3-dependent and augmented target genes during viral infection. Genes Immun 9, 168–175 (2008). [PubMed: 18094709]
18. Grandvaux N et al. Transcriptional profiling of interferon regulatory factor 3 target genes: direct involvement in the regulation of interferon-stimulated genes. J Virol 76, 5532–5539 (2002). [PubMed: 11991981]
19. Kühn R, Schwenk F, Aguet M & Rajewsky K Inducible gene targeting in mice. Science 269, 1427–1429 (1995). [PubMed: 7660125]
20. Epelman S et al. Embryonic and adult-derived resident cardiac macrophages are maintained through distinct mechanisms at steady state and during inflammation. Immunity 40, 91–104 (2014). [PubMed: 24439267]
21. Liu S et al. Phosphorylation of innate immune adaptor proteins MAVS, STING, and TRIF induces IRF3 activation. Science 347, aaa2630 (2015). [PubMed: 25636800]
22. Takeda K & Akira S TLR signaling pathways. Semin Immunol 16, 3–9 (2004). [PubMed: 14751757]
23. Yoneyama M & Fujita T RNA recognition and signal transduction by RIG-I-like receptors. Immunol Rev 227, 54–65 (2009). [PubMed: 19120475]
24. Sauer JD et al. The N-ethyl-N-nitrosourea-induced Goldenticket mouse mutant reveals an essential function of Sting in the in vivo interferon response to Listeria monocytogenes and cyclic dinucleotides. Infect Immun 79, 688–694 (2011). [PubMed: 21098106]
25. Manzanillo PS, Shiloh MU, Portnoy DA & Cox JS Mycobacterium tuberculosis activates the DNA-dependent cytosolic surveillance pathway within macrophages. Cell Host Microbe 11, 469–480 (2012). [PubMed: 22607800]
26. Hasan M et al. Trex1 regulates lysosomal biogenesis and interferon-independent activation of antiviral genes. Nat Immunol 14, 61–71 (2013). [PubMed: 23160154]
27. Essers MA et al. IFNalpha activates dormant haematopoietic stem cells in vivo. Nature 458, 904–908 (2009). [PubMed: 19212321]
28. Heymans S et al. Inhibition of plasminogen activators or matrix metalloproteinases prevents cardiac rupture but impairs therapeutic angiogenesis and causes cardiac failure. Nat Med 5, 1135–1142 (1999). [PubMed: 10502816]
29. Corrales L & Gajewski TF Molecular Pathways: Targeting the Stimulator of Interferon Genes (STING) in the Immunotherapy of Cancer. Clin Cancer Res (2015).
30. Fu J et al. STING agonist formulated cancer vaccines can cure established tumors resistant to PD-1 blockade. Sci Transl Med 7, 283ra52 (2015).
31. Hanson MC et al. Nanoparticulate STING agonists are potent lymph node-targeted vaccine adjuvants. J Clin Invest 125, 2532–2546 (2015). [PubMed: 25938786]
32. Furie R et al. Anifrolumab, an Anti-Interferon-α Receptor Monoclonal Antibody, in Moderate-to-Severe Systemic Lupus Erythematosus. Arthritis Rheumatol 69, 376–386 (2017). [PubMed: 28130918]
33. Khamashta M et al. Sifalimumab, an anti-interferon-α monoclonal antibody, in moderate to severe systemic lupus erythematosus: a randomised, double-blind, placebo-controlled study. Ann Rheum Dis 75, 1909–1916 (2016). [PubMed: 27009916]
34. Goldberg A et al. Dose-escalation of human anti-interferon-α receptor monoclonal antibody MEDI-546 in subjects with systemic sclerosis: a phase 1, multicenter, open label study. Arthritis Res Ther 16, R57 (2014). [PubMed: 24559157]
35. Muzumdar MD, Tasic B, Miyamichi K, Li L & Luo L A global double-fluorescent Cre reporter mouse. Genesis 45, 593–605 (2007). [PubMed: 17868096]

36. Sun Q et al. The specific and essential role of MAVS in antiviral innate immune responses. Immunity 24, 633–642 (2006). [PubMed: 16713980]
37. Hoebe K et al. Identification of Lps2 as a key transducer of MyD88-independent TIR signalling. Nature 424, 743–748 (2003). [PubMed: 12872135]
38. Sato M et al. Distinct and essential roles of transcription factors IRF-3 and IRF-7 in response to viruses for IFN-alpha/beta gene induction. Immunity 13, 539–548 (2000). [PubMed: 11070172]
39. Kamran P et al. Parabiosis in mice: a detailed protocol. J. Vis. Exp (80), e50556 (2013).
40. Dobin A et al. STAR: ultrafast universal RNA-seq aligner. Bioinformatics 29, 15–21 (2013). [PubMed: 23104886]
41. Anders S, Pyl PT & Huber W HTSeq--a Python framework to work with high-throughput sequencing data. Bioinformatics 31, 166–169 (2015). [PubMed: 25260700]
42. Robinson MD, McCarthy DJ & Smyth GK edgeR: a Bioconductor package for differential expression analysis of digital gene expression data. Bioinformatics 26, 139–140 (2010). [PubMed: 19910308]
43. Anders S et al. Count-based differential expression analysis of RNA sequencing data using R and Bioconductor. Nat Protoc 8, 1765–1786 (2013). [PubMed: 23975260]
44. Huang DW, Sherman BT & Lempicki RA Systematic and integrative analysis of large gene lists using DAVID bioinformatics resources. Nat Protoc 4, 44–57 (2009). [PubMed: 19131956]
45. Huang DW, Sherman BT & Lempicki RA Bioinformatics enrichment tools: paths toward the comprehensive functional analysis of large gene lists. Nucleic Acids Res 37, 1–13 (2009). [PubMed: 19033363]
46. Ahn J, Gutman D, Saijo S & Barber GN STING manifests self DNA-dependent inflammatory disease. Proc Natl Acad Sci U S A 109, 19386–19391 (2012). [PubMed: 23132945]
47. Schoggins JW et al. Pan-viral specificity of IFN-induced genes reveals new roles for cGAS in innate immunity. Nature 505, 691–695 (2014). [PubMed: 24284630]
48. Zilionis R et al. Single-cell barcoding and sequencing using droplet microfluidics. Nat Protoc 12, 44–73 (2017). [PubMed: 27929523]
49. Klein AM et al. Droplet barcoding for single-cell transcriptomics applied to embryonic stem cells. Cell 161, 1187–1201 (2015). [PubMed: 26000487]
50. Satija R, Farrell JA, Gennert D, Schier AF & Regev A Spatial reconstruction of single-cell gene expression data. Nat Biotechnol 33, 495–502 (2015). [PubMed: 25867923]
51. Aguirre AD, Vinegoni C, Sebas M & Weissleder R Intravital imaging of cardiac function at the single-cell level. Proc Natl Acad Sci U S A 111, 11257–11262 (2014). [PubMed: 25053815]
52. Lee S et al. Real-time in vivo imaging of the beating mouse heart at microscopic resolution. Nat Commun 3, 1054 (2012). [PubMed: 22968700]

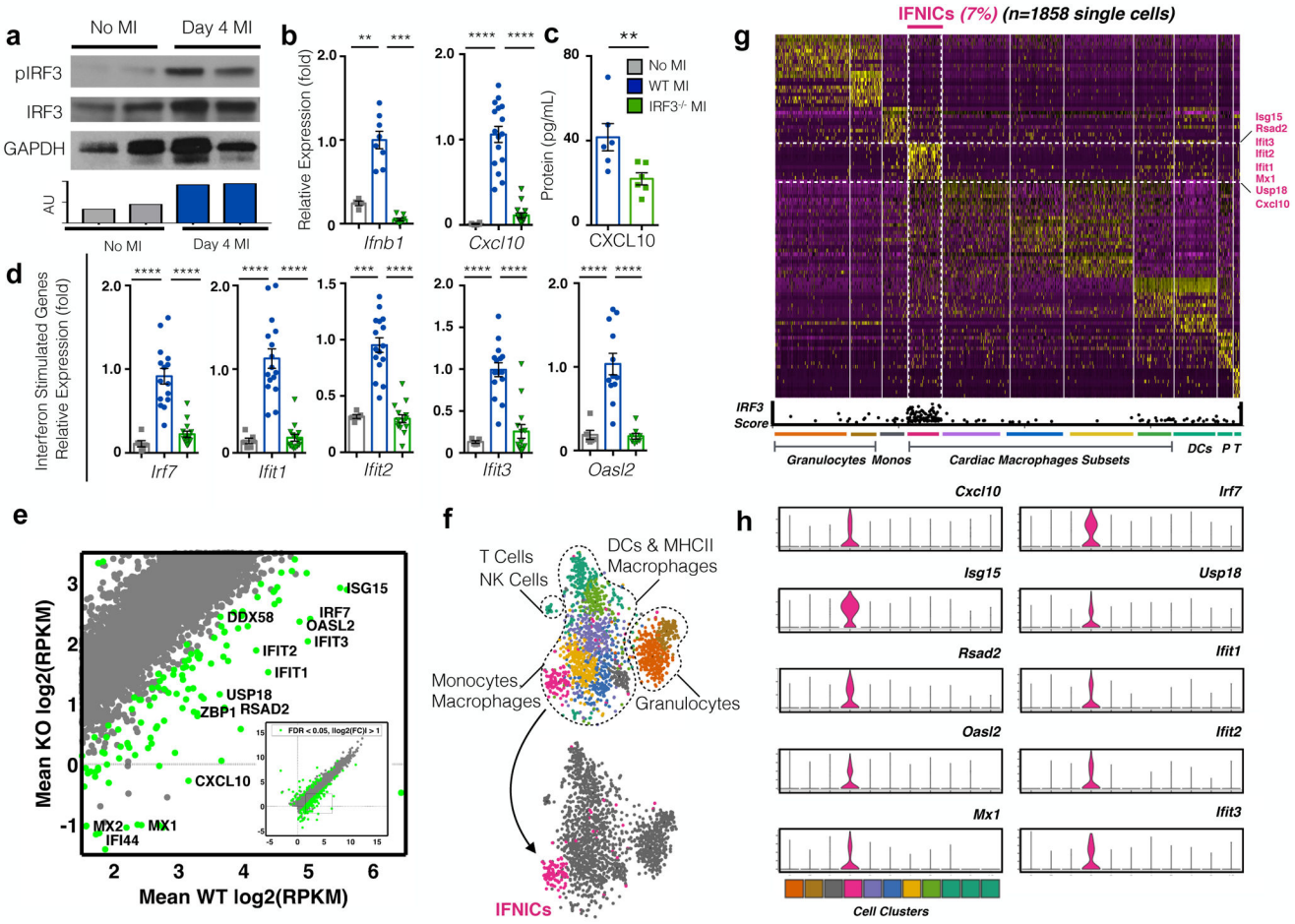

Figure 1.

Myocardial infarction activates IRF3-dependent signaling. **(a)** Immunoblotting for phosphorylated and total IRF3 without MI or at day 4 after MI (top) and semiquantitation of band intensities (bottom). GAPDH was used as a loading control (n=4 mice, 2 per group, from 1 experiment, 3 separate blots) AU, arbitrary units. **(b-d)** Levels in WT and *Irf3*$^{-/-}$ mice at day 4 after MI of *Ifnb1* (n=8 per group) and *Cxcl10* (n=15 *WT* and n=16 *Irf3*$^{-/-}$ mice) **(b)**, CXCL10 protein (n=6 per group) (**c**), and type I interferon-stimulated genes (ISGs) (n=15 *WT* and n=16 *Irf3*$^{-/-}$ mice) (**d**). Non-infarcted WT mice were used as a control in **b** and **d**. **(e)** Scatterplot of RNA-seq expression data from the infarct tissue of *WT* and *Irf3*$^{-/-}$ mice at day 4 after MI (n=3 mice per group). Differentially expressed genes are shown in green and several highly differentially expressed ISGs are annotated. Inset shows the full scatterplot for all genes. **(f)** Single cell RNA-Seq data from cells isolated from the infarct region of WT mice at day 4 after MI (n=1858 single cells from 1 wild type mouse). The data are displayed as color-coded clusters on a t-distributed stochastic neighbor embedding (tSNE) plot. The interferon inducible cell (IFNIC) cluster shown in pink is defined based in which 8 out of 10 discriminating marker genes are interferon stimulated genes. (IFNICs = Interferon inducible cells, DCs = dendritic cells, MHCII macrophages = major histocompatibility complex molecules) **(g)** Top, heat map plotting the top 10 marker genes for each cluster (y axis) versus single cells grouped by clusters (x axis). The IFNIC

population is indicated at the top of the heat map and selected marker genes are annotated on the right. Bottom, scatterplot showing the *IRF3 Score* for each cell (see Online Methods). (Monos = Monocytes, DCs = dendritic cells, P=proliferating cells, and T = T cells and natural killer cells) **(h)** Violin plots depicting the expression probability distribution for each single cell cluster. Ten IRF3-dependent genes are shown. Data are mean ± SEM. ** $P < 0.01$, *** $P < 0.001$, **** $P < 0.0001$.

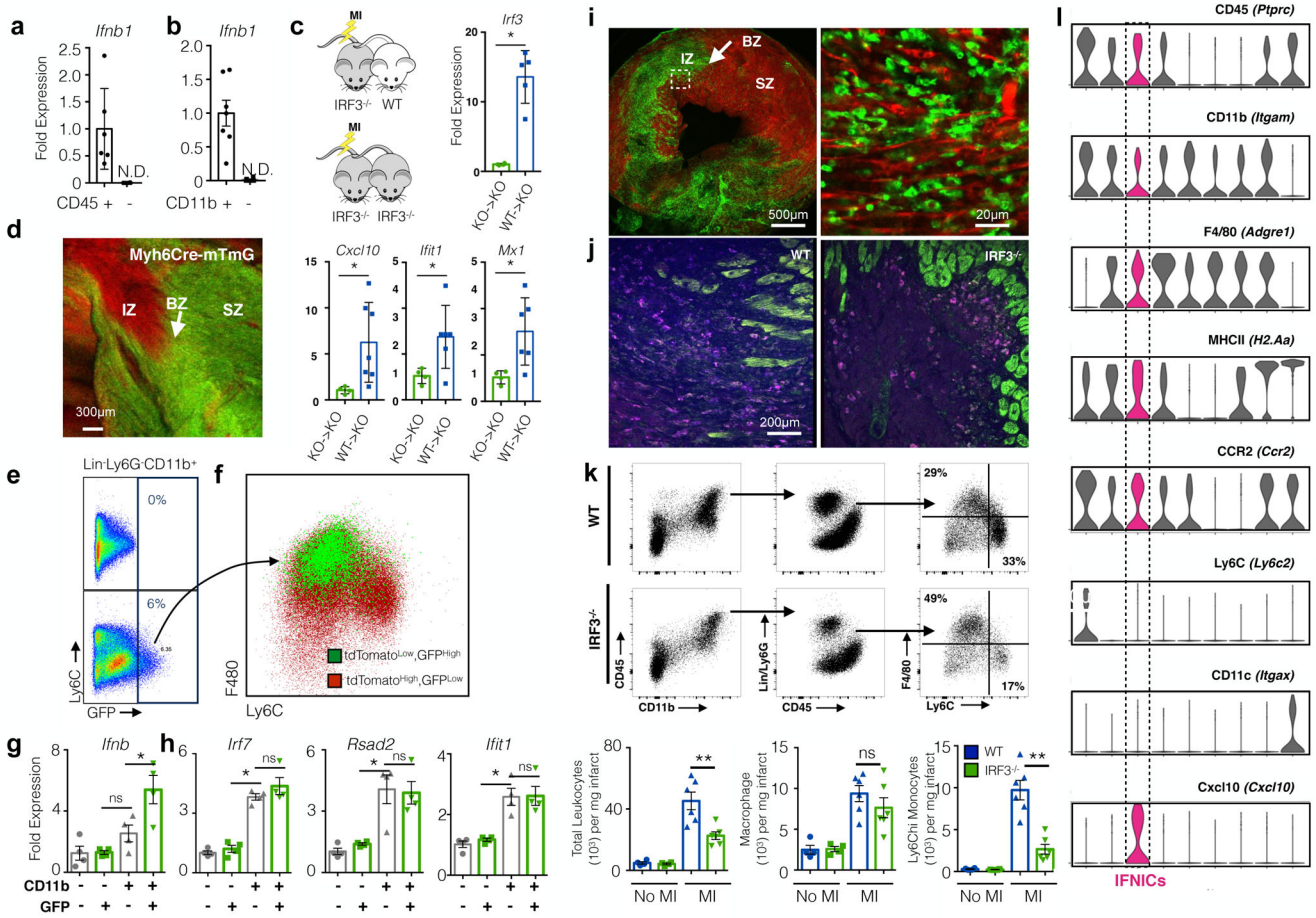

Figure 2.

Post-phagocytic macrophages initiate IRF3-dependent amplification of post-MI inflammation. **(a,b)** Relative *Ifnb1* expression levels in CD45+ and CD45- (n=6 per group) (**a**) and CD11b+ and CD11b- (n=6 per group) (**b**) cell populations sorted from infarct tissue of WT mice on day 4 after MI. **(c)** Schematic of a parabiosis experiment in which *Irf3*$^{-/-}$ mice were subjected to MI after they had been paired to either *Irf3*$^{-/-}$ (KO→KO) or WT (WT→KO) mice (left). Expression of the indicated IRF3-dependent genes in the heart of the *Irf3*$^{-/-}$ parabiont that underwent MI at day 4 after MI (n=4 KO->KO and n=5 WT->KO parabionts) (right and below). **(d)** Micrograph of the borderzone (BZ, arrow) of the heart of an *Myh6Cre-mTmG* reporter mouse on day 4 after MI; in these mice, cardiomyocytes express membrane EGFP (green) and all other cells express membrane tdTomato (red). IZ, infarct zone; SZ, survival zone. **(e)** Representative plots illustrating the gating strategy of Lin-Ly6G-CF11b+ myeloid cells used to identify post-phagocytotic macrophages that are associated with cardiomyocyte-derived DAMPs in *Myh6Cre-mTmG* mice. Cre negative reporters (top left) define GFP autofluorescence (0% cells above GFP threshold). Myh6Cre positive reporters (bottom left) exhibit 6% of cells above GFP fluorescence. **(f)** Representative backgating plot of the 6% GFP+ myeloid cells (arrow from gate to green overlay) on the GFP- myeloid population (red) from a Cre- mouse at day 4 after MI. Arrow indicates the gating strategy used to identify the GFP+ population. **(g,h)** Expression of *Ifnb1*

(**g**) and the indicated ISGs **(h)** in FACS sorted subpopulations based on CD11b and GFP status (representative of 2 experiments, n=4 mice each). **(i)** Fluorescence imaging of a short axis heart section from *Mx1Cre-mTmG* reporter mice on day 4 after MI, showing non-induced tdTomato expressing cells (red) and IFN-induced EGFP expressing cells (green). Low (left) and high (right) magnification are shown. **(j)** *Ex vivo* 2- photon autofluorescence imaging of infarct borderzone, showing surviving cardiomyocytes (green) and infiltrate (purple) in *WT* and *Irf3*$^{-/-}$ mice. **(k)** Gating strategy (top and middle) and leukocyte subset enumeration (bottom; total leukocytes, Lin^{-}CD11b^{+}F4/80^{high}Ly6C^{low} macrophages, and Lin^{-}CD11b^{+}F4/80^{low}Ly6C^{high} monocytes) from infarcts of WT and IRF3$^{-/-}$ mice on day 4 after MI (representative of 2 experiments, n=5 per group). **(l)** Violin plots of single cell RNA-Seq data from day 4 MI hearts (n=1,585 cells) depicting the expression probability distribution of selected genes for each mononuclear cell cluster. Genes were selected based on established mononuclear cell subset marker genes. $^{*}P < 0.05$, $^{**}P < 0.01$.

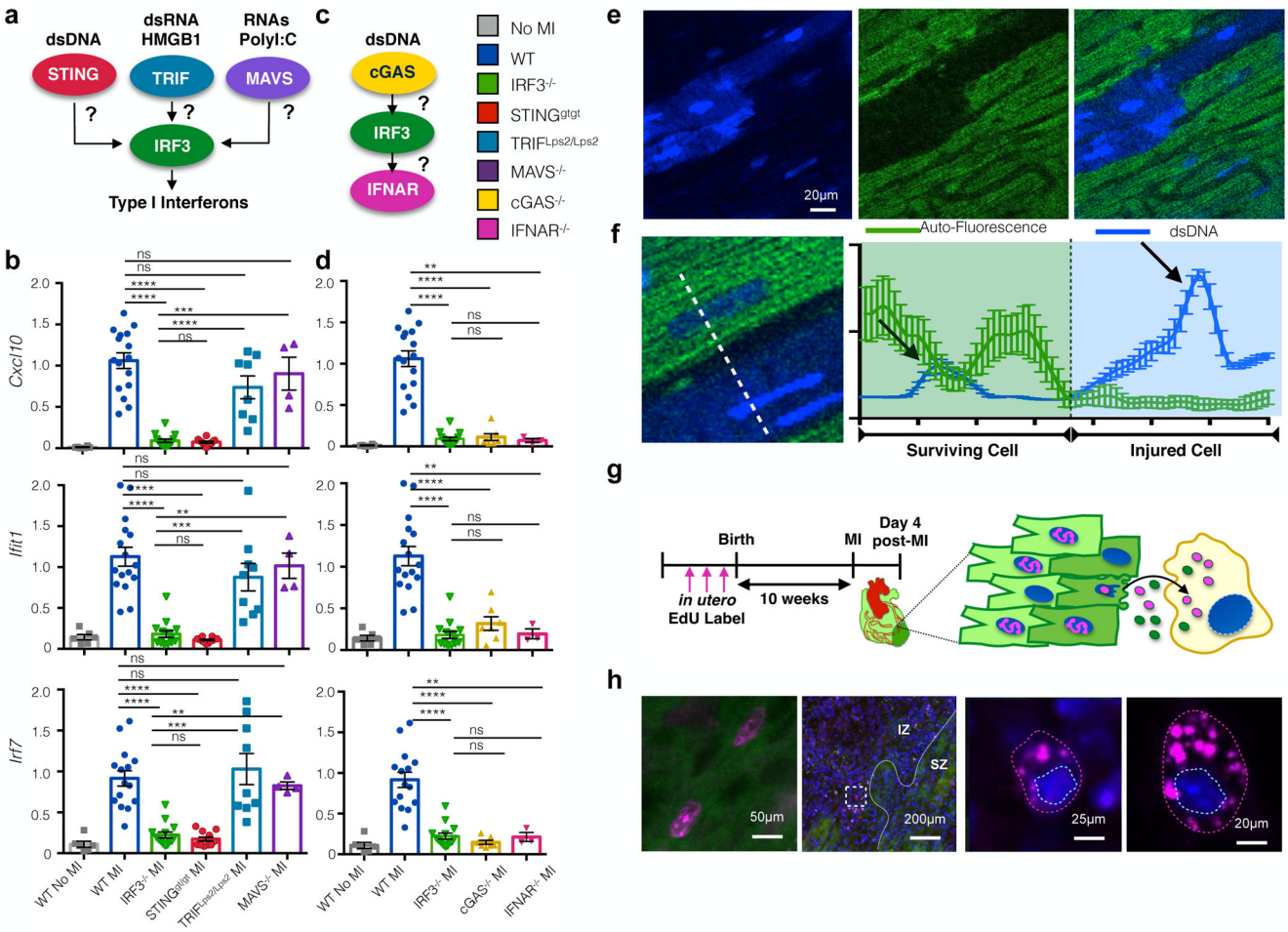

Figure 3.

Self DNA is the dominant MI-induced IRF3-activating DAMP. **(a)** Schematic of the three known IRF3 activation pathways, their respective adaptor proteins (TRIF, STING, and MAVS), and their proximal activating DAMPs. **(b)** Expression of *Cxcl10, Ifit1, and Irf7* in the infarct region at day 4 after MI in *WT* (n=16), *Irf3*$^{-/-}$ (n=15), *Trif*^{Lps2} (n=9), *Mavs*$^{-/-}$ (n=4), and *STING*$^{gt/gt}$ (n=12) mice, as compared to no MI in WT mice (n=4). **(c)** Schematic of the cytosolic DNA sensing pathway involving the DNA sensor cGAS, the transcription factor IRF3, and the type I interferon receptor IFNAR. **(d)** Expression of *Cxcl10, Ifit1, and Irf7* in the infarct region on day 4 after MI from *WT* (n=16), *Irf3*$^{-/-}$(n=15), *cGAS*$^{-/-}$ (n=7), and *Ifnar*$^{-/-}$ (n=4) mice, as compared to no MI in WT mice (n=4). Data are mean ± SEM. ** $P < 0.01$, *** $P < 0.001$, **** $P < 0.0001$. **(e)** Intravital multiphoton microscopy of WT mouse after coronary ligation showing localization of the double-stranded, DNA-specific fluorescent probe SYTOX Orange (blue, left), autofluorescence of surviving cardiomyocytes (green, middle), and overlay (right) after 20 minutes of ischemia-reperfusion. **(f)** Quantification of dsDNA probe fluorescence and cardiomyocyte autofluorescence along the linescan (dotted line) at the level of the nucleus spanning surviving and injured cardiomyocytes. Arrows indicates nuclear DNA staining. (x axis is distance, y axis is arbitrary fluorescence units along the dotted line) **(g)** Experimental strategy. WT mouse

cardiomyocytes were labeled *in utero by* EdU, such that the resulting adult mice have non-proliferative cardiomyocytes that retain EdU, whereas proliferative leukocytes dilute the EdU label. At 10 weeks of age, EdU labeled mice were subjected to MI; infarct tissue was harvested on day 4 and evaluated for EdU staining in the cytoplasm of infiltrating leukocytes. **(h)** EdU click-labeled to a fluorophore (purple) in autofluorescent cardiomyocytes (green) prior to MI (left) and in the borderzone of the infarcted heart, which contains EdU-positive debris (middle left). A magnified view (middle right) of the region indicated by the dashed box shows a cell (outlined with purple dots) with extranuclear EdU puncta (pink); the nucleus (outlined with white dots) is stained with a Hoechst nuclear stain (blue). EdU staining of a bone marrow derived macrophage after uptake of EdU-labeled cardiomyocyte DNA *in vitro* is shown for comparison (right).

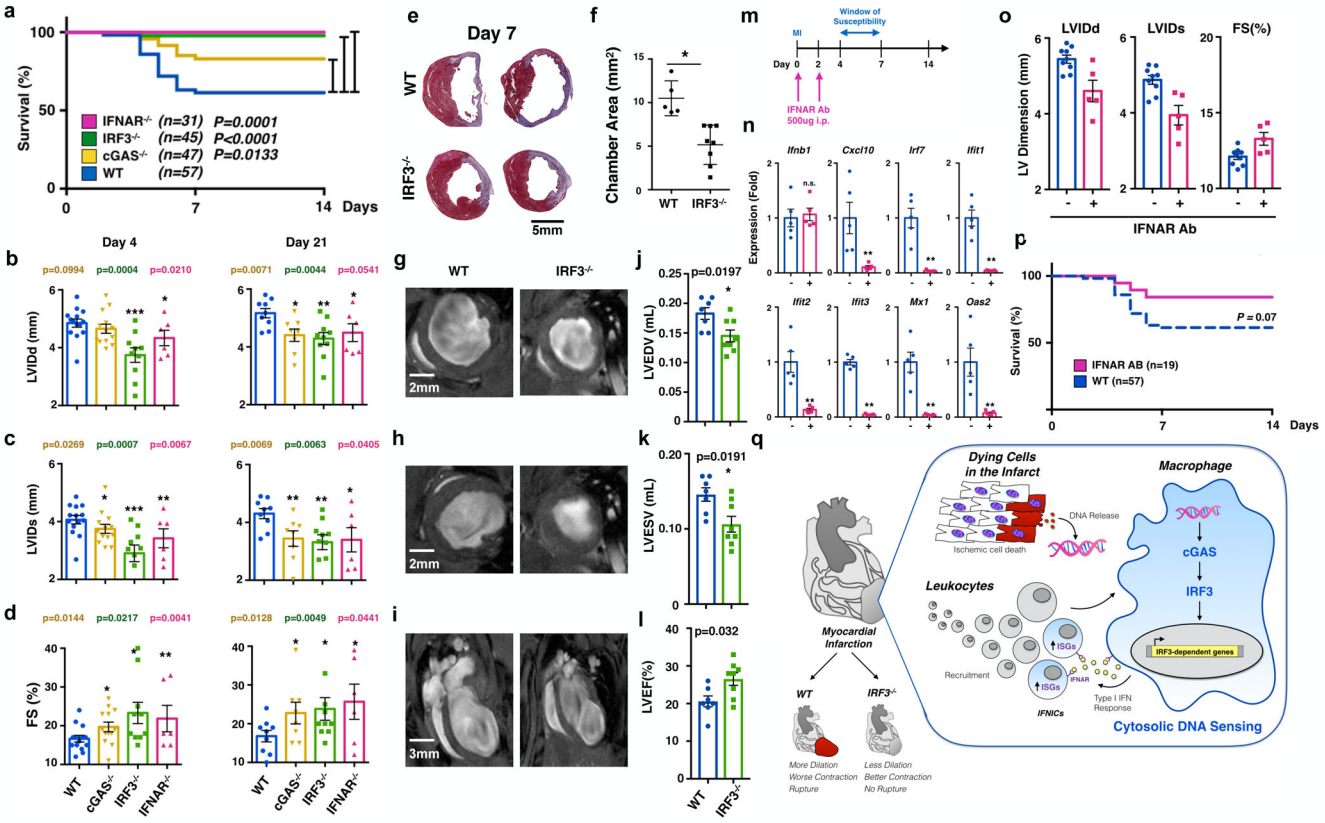

Figure 4.

Genetic and pharmacologic disruption of DNA-induced IRF3 activation and type I interferon signaling protects mice from death and adverse ventricular remodeling following MI. **(a)** Kaplan-Meier survival curves comparing post-MI survival of *WT* mice (n=57) to *cGAS*$^{-/-}$ (n=47, *P*=0.0133), *Irf3*$^{-/-}$ (n=45, *P*<0.0001) and *Ifnar*$^{-/-}$(n=31, *P*=0.0001) mice. (**b-d**). M-mode quantitation of echocardiographic parameters of the indicated mouse strains at days 4 and 21 after MI: left ventricular inner diameter at end-diastole (LVIDd) **(b)**, left ventricular inner diameter at end-systole (LVIDs) **(c)**, and fractional shortening (FS %) **(d)**. For each genotype, P values and n numbers (n=WT, knockout) are indicated. **(e)** Masson's Trichrome stain of short axis sections taken 1 mm below the suture ligation from *WT* (n=5) and *Irf3*$^{-/-}$ (n=7) mice on day 7 after MI. **(f)** Quantification of short axis chamber area 1 mm below the suture ligation on day 7 after MI. **(g-i)** Cardiac MRI of *WT* and *Irf3*$^{-/-}$ mice on day 21 after MI. Short axis images are shown at the level of the papillary muscle at end diastole **(g)** and end systole **(h)**, and 4-chamber long axis images are shown at end diastole (**i**). **(j-l)** Cardiac MRI-based quantification of left ventricular end-diastolic volume (LVEDV) **(j)**, left ventricular end-systolic volume (LVESV) **(k)**, and left ventricular ejection fraction (LVEF) **(l)** in *WT* (n=7) and *Irf3*$^{-/-}$(n=8) mice on day 21 after MI. **(m)** Experimental strategy. WT mice were treated with an IFNAR neutralizing antibody at 8–12 hr and 48 h after MI. **(n)** Expression of *Ifnb1* and ISGs at 4 days after MI in antibody-treated or untreated mice (n=4 per group) **(o)** Left ventricular diameters (LVIDd, LVIDs) and fractional shortening (%FS) at 21 days after MI (n=6 per group). **(p)** Kaplan-Meier survival curves comparing antibody-treated to untreated (WT) mice (n=19 IFNAR Ab, n=57 WT)). Data are mean ± SEM. *P <

0.05, ** $P < 0.01$, *** $P < 0.001$. **(q)** Working model for IRF3 activation after myocardial infarction.